Self-powered near-infrared photodiode based on a $MoSe_2/MoS_2$ heterojunction

Oscar A. López-Galán,* Nestor Perea, John Nogan, Marco Ramirez, Danilo Nagaoka, Amanda Carrillo Castillo, Mauricio Terrones, Delphine Chassaing, Martin Heilmaier, Pamela Pineda, and Manuel Ramos*

Received: 15 July 2026 / Accepted: 4 October 2026

We report on the fabrication of a low-cost $MoSe_2/MoS_2$ thin-film heterojunction on a *p*-type Si wafer with near-infrared (NIR) detection capabilities using low-temperature radio frequency (RF) sputtering with commercial targets. The device operates as a *p–n* photodiode at room temperature, with evidence of the creation of a *p–n* junction with rectification ratios of 10^3 and ideality factors of ~2.5. Under reverse-bias operation, the device has photogenerated currents of up to 65 nA, reaches a maximum photoresponsivity of 0.045 μA W^{-1}, and detectivities of up to 1.1×10^5 Jones. Moreover, the device can function as a self-powered photodetector with photogenerated currents of up to 16 nA with a photoresponsivity of 0.003 μA W^{-1} at 980 nm and detectivities in the order of 10^4 Jones. This work proves that facile, affordable, and compelling near-IR photodetectors can be fabricated using transition metal dichalcogenides integrated with Si technology and RF sputtering.

Impact statement

Scalable fabrication by radio frequency sputtering of a self-powered infrared photodiode, which means it can detect IR signals without an applied voltage. The device is formed from an *n*-type $MoS_2/MoSe_2$ thin-film heterojunction directly deposited on a commercial *p*-type Si wafer.
The electrical characteristics of the device indicate the formation of a *p–n* junction that creates a built-in potential. This built-in potential effectively separates the photogenerated charge carriers and permits the self-powered capacity of the device.
Additionally, the results demonstrate a compelling performance that can compete with commercially available versions of infrared detectors, with the additional advantage of working without cooling systems and under low-power operation conditions.

Introduction

Developing high-performance, cost-effective, and versatile infrared (IR) photodetectors is a crucial technological driver across fields such as security surveillance, astronomical observation, medical diagnostics, and consumer electronics.[1,2] Current IR research relies on Si, InGaAs-based, two-dimensional (2D) materials, and multilayer photodetectors[3–5] and, more notably, on commercial HgCdTe photodetectors, which require a cooling system that limits their broad application and miniaturization, in addition to the rigidity and fragility of such devices. These constraints motivate the development of high operating temperature (HOT) devices, capable of functioning at temperatures above 120 K with reasonable metrics.[6–8] Therefore, the research for new materials and structures capable of next-generation features, such as minimum power consumption, self-powered operation, and integration with silicon (Si), is a

Oscar A. López-Galán, Departamento de Física y Matemáticas, Instituto de Ingeniería y Tecnología, Universidad Autónoma de Ciudad Juárez, 450 Avenida del Charro, 32310 Ciudad Juárez, Chihuahua, México; Department of Industrial, Manufacturing and Systems Engineering, The University of Texas at El Paso, El Paso, TX 79968, USA; oscar.lopez@uacj.mx
Nestor Perea, Department of Physics, Penn State University, University Park, PA 16802, USA
John Nogan, Center for Integrated Nanotechnologies (CINT), Sandia National Laboratories, 1101 Eubank Bldg. SE, Albuquerque, NM 87110, USA
Marco Ramirez, Department of Chemistry and Biochemistry, The University of Texas at El Paso, El Paso, TX 79968, USA
Danilo Nagaoka, Department of Physics, Penn State University, University Park, PA 16802, USA
Amanda Carrillo Castillo, Departamento de Eléctrica y Computación, Instituto de Ingeniería y Tecnología, Universidad Autónoma de Ciudad Juárez, 450 Avenida del Charro, 32310 Ciudad Juárez, Chihuahua, México
Mauricio Terrones, Department of Physics, Penn State University, University Park, PA 16802, USA; Department of Materials Science and Engineering, Penn State University, University Park, PA 16802, USA
Delphine Chassaing, Institute for Applied Materials and Materials Science, Karlsruhe Institute of Technology (KIT), Engelbert-Arnold-Str. 4, 76131 Karlsruhe, Germany
Martin Heilmaier, Institute for Applied Materials and Materials Science, Karlsruhe Institute of Technology (KIT), Engelbert-Arnold-Str. 4, 76131 Karlsruhe, Germany
Pamela Pineda, Departamento de Física y Matemáticas, Instituto de Ingeniería y Tecnología, Universidad Autónoma de Ciudad Juárez, 450 Avenida del Charro, 32310 Ciudad Juárez, Chihuahua, México
Manuel Ramos, Departamento de Física y Matemáticas, Instituto de Ingeniería y Tecnología, Universidad Autónoma de Ciudad Juárez, 450 Avenida del Charro, 32310 Ciudad Juárez, Chihuahua, México; manuel.ramos@uacj.mx
*Corresponding author
doi:10.1557/s43577-026-01233-5

© The Author(s) 2026

fundamental challenge in the field of materials research and IR technology.

While recent advances in 2D devices based on MoS_2 and other TMDCs demonstrate outstanding figure-of-merit parameters, such as a near-unity rectification ratio[9] and detectivities above 10^{12} Jones,[10,11] 2D devices still rely on complex, unscalable fabrication methods for large-scale production and lack tuning for IR detection.[4] For instance, Dai et al. fabricated a MoS_2 Schottky diode capable of detecting 980 nm with remarkable detectivity and responsivity.[12] Likewise, Shin et al. tested a Si–MoS_2 *p–n* photodiode with a responsivity and detectivity of 76.1 A W^{-1} and 10^{12} Jones.[13] However, their fabrication methodologies rely on mechanically exfoliated MoS_2 flakes transferred onto a following layer or substrate.

Thin-film technology offers a mature, direct route to feasible applications for IR photodetectors that require a balance of performance, high reliability, and scalable manufacturing costs. Moreover, thin-film interface engineering has emerged as one of the most promising technologies for efficient, commercially viable light detection,[14,15] especially when integrated with current Si technology. This technology has enabled an enhancement of carrier transport and mobility in oxide thin-film transistors,[16] and improvements in defect passivation and conversion in Sb_2Se_3 and CdTe solar cells.[17–19] What is more, combining transition-metal dichalcogenides (TMDCs) with Si has been demonstrated by directly fabricating multilayered MoS_2 on Si[18,19] to detect 200- and 680-nm laser wavelengths. Recently, broadband $PtSe_2$-based photodetectors have been integrated with Si technology successfully,[20,21] similar to what Chávez-Urbiola et al. reported for a photodetector using an *n*-ZnO/*p*-Si heterostructure by RF sputtering, where the authors attribute the functioning of the device to the sole photovoltaic effect.[22] Khalil et al. fabricated a composite MoS_2/SiC thin film on Si with RF magnetron sputtering,[23] which shows great potential for large-scale production via physical deposition methods. Likewise, Ma et al. reported a multilayered $PtSe_2$/pyramid-Si heterostructure by using chemical vapor deposition and post-selenization.[24] Their device demonstrates a responsivity of 567 mA W^{-1} and a detectivity of 1.26×10^{13} at 800-nm wavelengths, highlighting the scalability of their method. Therefore, scalability, tuning IR detection, and large-area photodetection remain key factors to address in this area.

This work focuses on process control to enhance material quality and heterojunction formation, using commercially available RF-sputtering targets and Si technology. The goal is to develop device engineering for improved near-IR detection with a *p*-Si/$MoSe_2$/MoS_2 structure. Unlike recent reports on 2D devices and thin-film detectors, our device was easily integrated into a commercial *p*-type Si wafer. Additionally, we achieved proper performance at low voltages and room temperature, demonstrating photodetection capabilities under self-powered conditions. We consider that the primary mechanism of photogenerated current is the photovoltaic effect at the semiconductor junction, while the photo-thermoelectric contributions are minimized. These findings advance the development of IR technology and confirm the potential of RF-sputtered chalcogenide thin films for scalable device research and fabrication.

Results

$MoS_2/MoSe_2$ multilayer crystallinity

We used a two-step multilayer RF sputtering of MoS_2 and $MoSe_2$ that focused on repeatability and integration with commercial Si wafer technology. A cross-sectional scanning electron microscopy (SEM) image analysis of the MoS_2/$MoSe_2$ multilayer reveals a distinct and well-defined interface between the two layers, as shown in **Figure** 1a. The total film thickness is approximately 1.6 µm, with each TMDC layer measuring around 800 nm. The surface morphology exhibits a characteristic fringe-like texture (Figure 1b), consistent with the previous observations.[25,26] The latter suggests that this texture arises from the preferential growth of $MoSe_2$ and MoS_2 along the (100) crystallographic plane, resulting in vertically aligned layers of the TMD material. Raman spectroscopy further supports this vertical alignment as depicted in Figure 1c. Vibrational modes observed at 405 cm^{-1}, and ~377 cm^{-1} correspond to the A_{1g} and E^1_{2g} modes of MoS_2, respectively.[27–29] The intensity relationship between the A_{1g} and E^1_{2g} modes may suggest preferential grain orientation along the out-of-plane direction, reinforcing the presence of vertical alignment in the heterostructure.

We performed atom probe tomography on the MoS_2/$MoSe_2$ heterojunction to determine the chemical distribution of the MoS_2 and $MoSe_2$ just at the interface. The collected ion map along the vertical axis of the heterojunction confirms a well-defined interface formation, displaying two distinguishable regions (Figure 1d). The isosurface of S_2 concentration (6.8 at%) shows the boundary between the detection of S and Se ions with low intermixing detection. Furthermore, the proxigram (individual ions' counts as a function of distance) along the perpendicular direction of the isosurface (Figure 1e) displays a clear distinction between the detection of Se and S ions, indicating that a small intermixing of species occurs between the two materials.[30] Therefore, we demonstrate a scalable two-step RF-sputtering methodology for fabricating a multilayer $MoSe_2$/MoS_2 heterojunction.

p-Si/MoS_2/$MoSe_2$ diode

We confirm the existence of a depletion region between the Si substrate and our MoS_2/$MoSe_2$ heterojunction, for example, a *p–n* junction, by extracting a nonlinear current versus voltage (*I–V*) curve from −4 to 4 V with an on-voltage of ~0.75 V under dark conditions (I_{dark}) versus an applied voltage at the drain (V_D), as shown in **Figure** 2a. This rectification characteristic indicates that charge carriers flow easily between the tungsten tips used as electrodes due to near-ohmic contact behavior between the metal tips used and the device, and no ambipolar conduction is present.[31] Tungsten (W) has an approximate work function of 4.5 eV, which should create an ohmic contact with MoS_2 due

to the small work function difference.[12] The device exhibits a rectification ratio of 10^3 at $V_D = \pm 2$ V, and an ideality factor (n) of 2.56 was determined from the slope of the linear region of the semi-log plot of the I–V curve (inset Figure 2a). The ideality factor comes from the analysis of the I–V curve using the Shockley equation, which reads as follows:

$$I = I_{dark}\left(e^{\frac{qV_D}{nkT}} - 1\right), \quad (1)$$

where I_d is the saturation current, q is the elementary charge, k is the Boltzmann constant, and T is the absolute temperature. Near-unity values of n have only been achieved recently by Wen et al. in a single-layer $MoS_2/ZrTe_2$ Schottky diode with Pt contacts.[9] Similarly, Dai et al. achieved ideality factors of 1.15 in a MoS_2 Schottky diode, but with important scalability limitations due to the exfoliation and transfer processes used in fabricating the device. In this sense, our device represents a substantial advancement in device fabrication, as it presents an improved ideality factor compared to monolayer MoS_2/GaN, where n was reported to be 11,[10] MoS_2|ZnO isotype heterostructure diode with n values of ~3[32] or to NiO/Si diode, where it reaches values of up to ~9 as a function of available oxygen during device fabrication.[33] Recently, Roy et al. fabricated a graphene/Si nanowire heterostructure for near-IR detection (730-nm wavelength); their device presents an ideality factor of 2.9.[34] Our ideality factor, therefore, indicates a good interface quality achieved by our fabrication method and is reproducible (see Supplemental material). Although the existence of interface defects is still present and relates to our ideality factor, dark current in a p–n diode is mainly a consequence of radiative and nonradiative losses, for example, attributed to band-to-band recombination and nonradiative losses to Shockley–Read–Hall and Auger recombination[35]—high ideality factors can also indicate a facile formation of low-resistance ohmic contacts, as reported in AlGaN/GaN p–n junction diodes.[36] Further discussion on interface defects is presented in the following sections.

Besides, the device presented a power extraction of 0.12 mW at 3 V under dark conditions (Figure 2b). On the other hand, the recorded temperature-dependent I–V curves show that the measured current increases by an order of magnitude when the device is operated at 600 K under dark conditions (Figure 2c). A five fold increase in the measured current is observed at a temperature of 400 K. However, there is a noticeable increase in reverse current at 600 K up to -0.2×10^{-6} A due to an increased number of thermally activated charge carriers. Such charge carriers are swept away by the applied potential (Figure 2d), thereby contributing to the observed reverse conduction. The operation of the device under high temperatures highlights its stability as MoS_2 retains its layered crystal structure at temperatures up to 600 K.[37]

On the other hand, under dark conditions and at 300 K, a low reverse current of -1×10^{-10} A was observed in our device at reverse polarization, indicating bias-independent

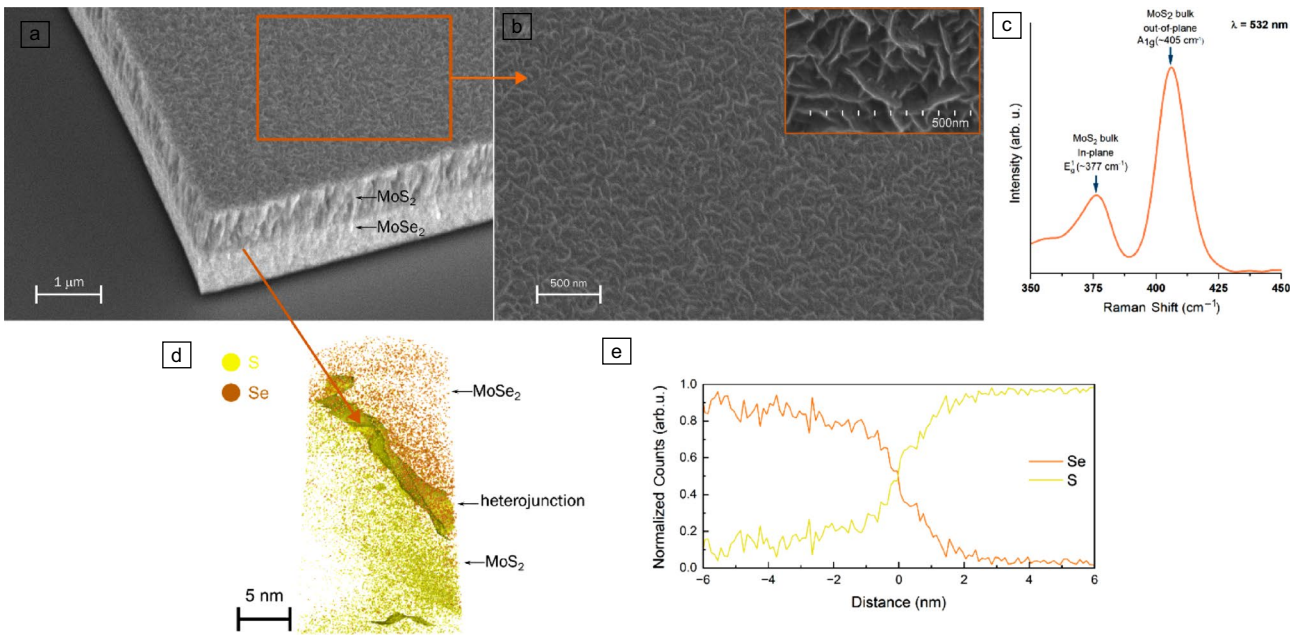


Figure 1. (a) Cross-section scanning electron microscopy (SEM) image from the deposited $MoSe_2/MoS_2$ heterojunction showing the two distinct materials and the formation of a well-distinguished interface. (b) Close-up SEM image showing the fringe-like morphological structure of the MoS_2. (c) Raman spectroscopy showing the characteristic Raman modes of MoS_2 and confirming the presence of the crystalline material. (d) Ion map resulting from the atom probe tomography of the $MoSe_2/MoS_2$ heterojunction. (e) Proxigram for 6.8 at% S concentration perpendicular to the isosurface.

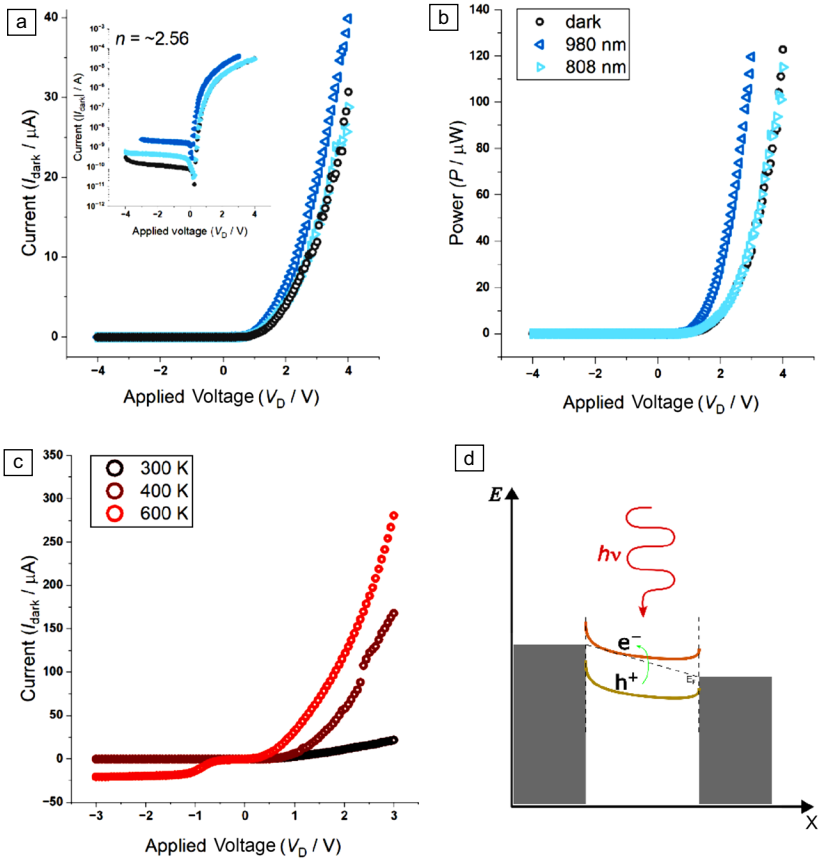


Figure 2. (a) *I–V* curves of the heterojunction measured under dark conditions and under illumination with the 980- and 808-nm laser wavelengths, inset: semi-log plot *I–V* considering the absolute value of the measured current under dark and under illumination, indicating an ideality factor of ~2.56, (b) Dissipated power of the device under dark and under illumination, (c) *I–V* curves of the heterojunction measured under dark conditions at temperatures of 300, 400, and 600 K. (d) Schematic showing that with an applied voltage V > 0 and an illumination source narrower than the semiconductor width.

behavior even at $V_D = -5$ V (Figure S1) and confirming that the classic thermionic emission model can successfully model carrier transport in our device.[9] One benefit of this low reverse current and moderate rectification ratio is the device's usability as a prototyping heterojunction photodetector. With these results, we then tested our device's capacity to function as a near-IR photodetector, as presented in the next section.

p-Si/MoS_2/$MoSe_2$ photodetection capacities

Observing the photocurrent (I_{ph}) response as a function of time at different laser power levels, our device exhibits photodetection capabilities at 980- and 808-nm wavelengths, achieving photocurrents of ~0.6 nA with distinct ON and OFF states, with an increase in photocurrent as the laser power increases, as depicted in **Figure** 3. Detection of weaker laser powers, up to 0.005 mW, was achieved at only 980-nm wavelength, with measured photocurrents of −0.15 nA (Figure S2). These electron–hole pairs generated by the incident radiation are separated and accelerated by the external electric field and hence contribute to conduction. A second mechanism of charge-carrier generation is the photo-thermoelectric effect (PTE), which occurs at metal–semiconductor interfaces. This effect arises from the temperature difference between a contact metal and the semiconductor, due to their different Seebeck coefficients, resulting in a generated current. This PTE contribution arises from a temperature gradient induced by light absorption and the generation of a photothermal voltage across the junction. Further details of the measurement performed are provided in the Methods section. This PTE contribution increases the values of figure-of-merit parameters in 2D devices, such as responsivity and detection limit, by several orders of magnitude, due to the large number of charge carriers injected from the metal contacts. We employ tungsten (W) tips to contact the device in our measurement setup, setting a gap between the electrodes wider than the laser spot (<2 μm) to guarantee that the PTE contribution from the contact to the overall detected photocurrent is minimal. Therefore, we consider that our device is primarily operated by PV-generated charge carriers, as illustrated in the schematic of Figure 3e–h. In these illustrations, we depict the widening of the depletion region and its corresponding energy diagram showing the separation of the Fermi levels by a value V_D, which is equal to our applied reverse bias. The schematic of the device under no applied bias shows a shortening of the depletion region, while its corresponding energy diagram indicates the separation of the Fermi levels by the built-in voltage at the junction.

Furthermore, figure-of-merit parameters, such as responsivity and detection limit, were evaluated to assess the device's performance, as done in previous studies.[10,35] The efficiency of a material to respond to the incident light is indicated by its photoresponsivity (R) and is given by the following:[38]

$$R = \frac{I_{ph} - I_d}{P_i},$$

where I_{ph} is the photocurrent generated at a given forward bias, and P_i is the laser power. For our device, the maximum photoresponsivity was ~0.045 μA W^{-1} at 980 nm (Figure 3c),

with slightly lower values at 808 nm. The extracted response time of our device was 100 ms, which is only doubled compared to those near-atomic dimensions using single-layer and few-layer arrangements[12] and represents an improvement compared to bulk $SnSe_2$ near-IR detectors,[39] considering the transition of carriers through the indirect bandgap. Our device's responsivity is comparable to that of previous $SnSe_2$/PEDOT:PSS photodetectors reported by Mukhokosi et al.,[40] and future improvements should focus on reducing trap states within the material's bandgap, for example, by heterogeneous integration of the device as reported recently by Gosh et al.[41]

The detection limit (D^*) is also a critical parameter representing the ability of the material to respond to low optical signals, and it can be estimated by using the shot-noise-limited expression[5,42]

$$D^* = \sqrt[R]{\frac{A}{2eI_d}},$$

where R is the responsivity, I_d is the dark current at a given forward bias, A is the area of the device where effective absorption of incident light occurs, and e is the electronic charge. Our device demonstrates the values of D^* up to 1.1×10^5 Jones at 1 mW of laser at a 980 nm wavelength. At an 808-nm laser wavelength of 1 mW, the device shows a detectivity of 0.9×10^5 Jones (Figure 3d). Our detectivity is substantially lower than 2D devices (**Table** I), for example, a GaSe/$MoSe_2$ selenide van der Waals photodetector[43] or 2D $PtSe_2$/Si-NWA photodetector.[44] However, because our device does not rely solely on the PTE occurring at metal–semiconductor interfaces, it can potentially function without cooling systems and avoid potential incremental losses and higher uncontrolled ideality factors due to temperature increase.[34,39]

p-Si/MoS_2/$MoSe_2$ self-powered photodetection capacities

Our device demonstrated self-powered detection by generating a measurable photocurrent at 0 V bias, with detectable ON and OFF states, up to 1 mW of power (**Figure** 4). The maximum generated photocurrent was 16 nA, observed with 980-nm laser illumination at 20 mW, representing almost four times less current than with an applied reverse bias. Under the conditions of illumination but no applied bias, the operation is performed by PV-generated charge carriers, and again, to a lesser degree by thermally generated carriers at 300 K. Because the main mechanism to separate the newly created electron–hole pairs is due to the built-in electric field, it is correct to assume that a higher recombination rate occurs just at the depletion region, decreasing the number of charge carriers detected. As depicted in Figure 3f, h, a wider separation of the Fermi levels under an applied reverse bias results in efficient separation of electron–hole pairs, compared to the built-in potential created by the p–n junction.[11,40,45] Then, before being collected in the corresponding electron diffusion and hole diffusion regions, they will eventually recombine. This explains the

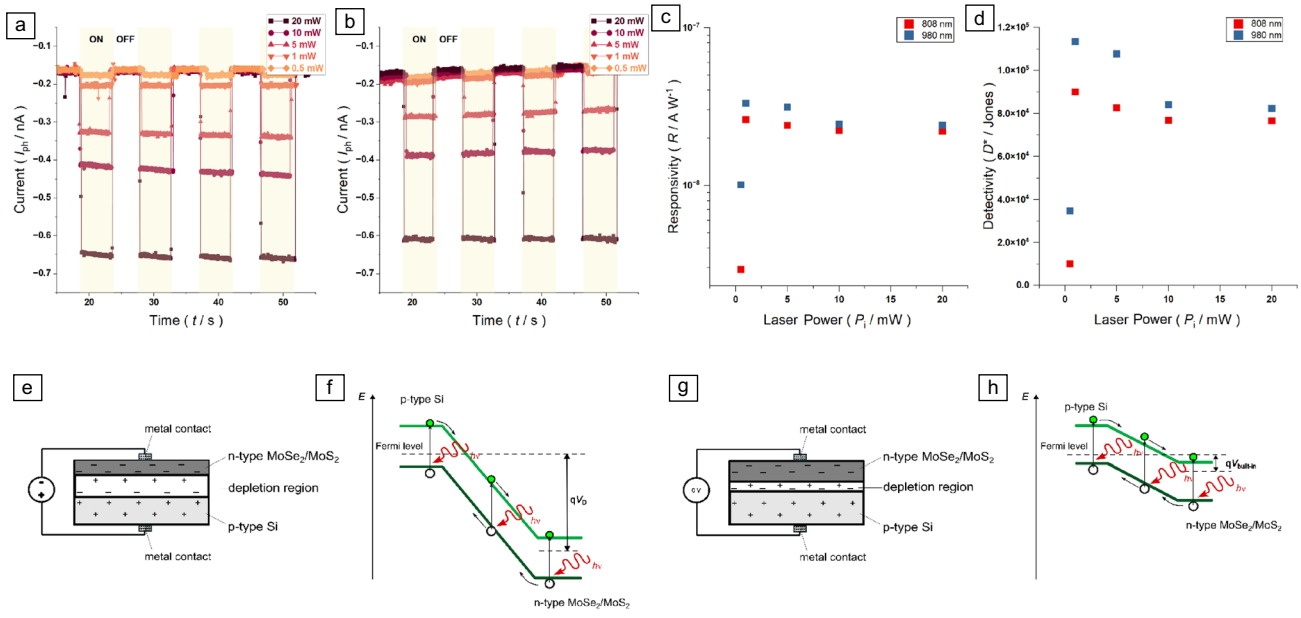


Figure 3. Time-resolved photoresponse of our p-Si/MoS_2/$MoSe_2$ device under applied reverse bias (–3 V) at (a) 980-nm laser illumination and (b) 808-nm laser illumination and under different laser powers. (c) Computed responsivity (R). (d) Computed detectivity (D^*), (e) schematic of the device under reverse bias, (f) corresponding energy diagram, (g) schematic of the device under no applied bias, and (h) corresponding energy diagram.

Table I. Comparative performance metrics of TMDC-based heterostructured photodetectors.

Device	Structure	Fabrication method	Operating wavelength (λ)	Responsivity (R)	Detectivity (D^*)	References
$PtSe_2$/Si-NWA	2D/3D vertical heterojunction on silicon nanowire arrays	CVD (selenization) and chemical etching	780 nm	12.65 A W^{-1}	2.5×10^{13} Jones	44
GaSe/$MoSe_2$	2D vDW heterojunction	Mechanical exfoliation	532 nm	0.169 A W^{-1}	2.8×10^{13} Jones	43
$PtSe_2$/Pyramid-Si	2D/3D vertical heterojunction array on 3D pyramidal microstructured Si	CVD (thermal selenization) and wet etching	808 nm	8.06 A W^{-1}	4.78×10^{13} Jones	24
p-Si/*n*-MoS_2	2D/3D vertical *p–n* heterojunction	Mechanical exfoliation and transfer to Si	660 nm/850 nm	76.1 A W^{-1}	1.60×10^{12} Jones	13
SiC/MoS_2	2D/3D composite thin-film *p–n* photodiode on Si substrate	RF sputtering	535 nm	63.22 mA W^{-1}	–	23
p-Si/*n*-MoS_2	thin-film *p–n* photodiode on Si substrate	RF sputtering	980 nm/800 nm	0.045 μA W^{-1}	1.1×10^5 Jones	This work

lower photocurrent in our device but can potentially guide future research towards improved self-powered operation, for example by tandem structures[1,46] or by front-end methods such as RF power or annealing tuning during fabrication.[47,48]

Moreover, the calculated responsivity of the device under self-powered photodetection diminishes by an order of magnitude for both wavelengths considered, reaching a value of up to ~0.003 μA W^{-1} at 980 nm. Likewise, the detectivity also reduces to 3×10^4 Jones and 1.5×10^4 Jones at 808 and 980 nm, respectively, which is an order of magnitude lower than the detectivity achieved under an applied bias. A similar behavior was reported by Chávez-Urbiola et al. when comparing their *n*-ZnO/*p*-Si photodetector under bias and under self-powered conditions.[22] Although the device exhibits solid performance comparable to commercial alternatives, for the wavelengths of 980 and 808 nm, it is capable of functioning as intended and, more importantly, under unbiased and room-temperature conditions. These results indicate that the *p*-Si/$MoSe_2$/MoS_2 heterojunction device can function as a photodetector at room temperature under reverse-bias conditions and under self-powered operations with reasonable metrics.

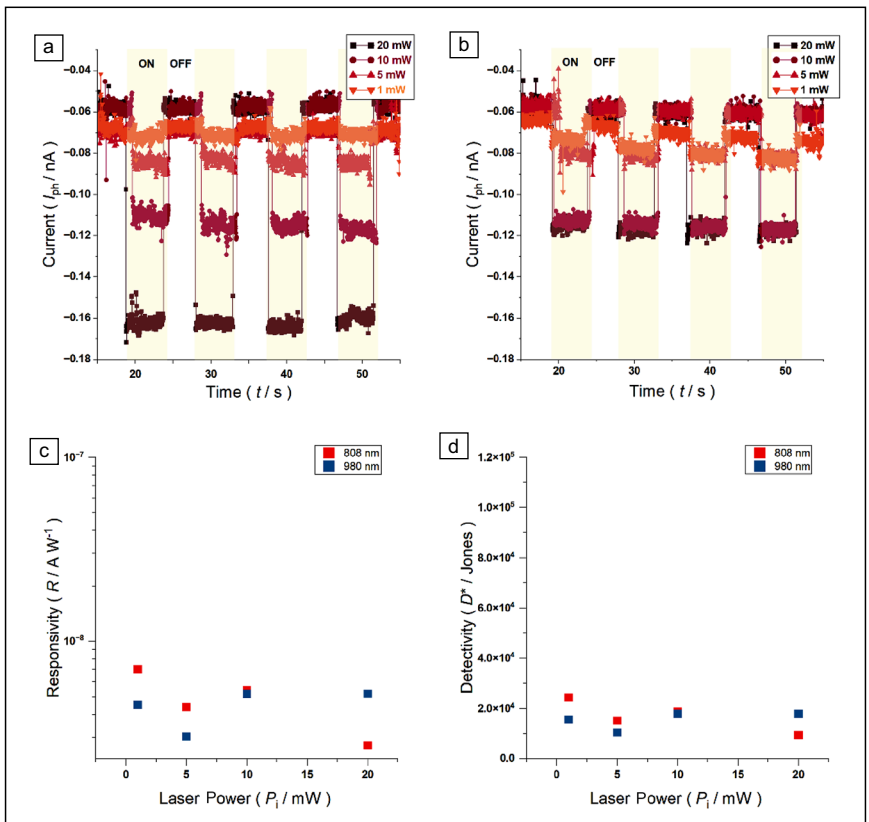


Figure 4. Time-resolved photoresponse of our p-Si/MoS_2/$MoSe_2$ device under no applied bias (self-powered) at (a) 980-nm laser illumination and (b) 808-nm laser illumination and under different laser powers, (c) Computed responsivity (R), and (d) Computed detectivity (D^*).

Capacitance versus voltage measurements

To better understand the elevated ideality factor and estimate defect densities, we performed

capacitance–voltage (C–V) measurements of our device under dark conditions and at room temperature across multiple frequencies (**Figure** 5). Given our device configuration, we apply a positive voltage to the cathode relative to the anode. The C–V curve shows a flat region in forward bias (indicated by $V_D < 0$ V), with values of approximately 46 pF at 100 kHz and 85 pF at 10 kHz, and a sharp frequency dispersion as frequency increases. As the applied voltage increases into the reverse-bias regime ($V_D > 0$ V), the capacitance decreases steeply, consistent with the widening of the depletion region in a standard diode structure.[32,49]

By looking at the Mott–Schottky plot of $1/C^2$ versus V_D for 10, 50, and 100 kHz (Figure 5b), we determined the slope $S(f)$ at each frequency. Then we extracted the interface trap density (D_{it}) from the slope difference between 10 and 100 kHz using the following relation (details provided in the supplemental material):

$$D_{it} \approx \frac{\Delta C}{qA},$$

where q is the elementary charge and A is the active device area. This resulted in an estimated D_{it} of 7.458×10^{13} cm^{-2}, confirming excess interface capacitance (C_{it}) charging through defect states in our device at lower frequencies. Moreover, the effective carrier density $N_{eff}(f)$ at each frequency can be estimated using the following expression:[50]

$$N_{eff}(f) = \frac{2}{q\epsilon A^2 S(f)},$$

where ϵ is the relative permittivity. This resulted in a N_{eff} (10 kHz) of 8.56×10^{13} cm^{-3} and a N_{eff} (100 kHz) of 5.37×10^{13} cm^{-3}. Because deep traps lying near the middle of the bandgap can respond to the 10 kHz signal but freeze out at 100 kHz, leaving only the response of the shallow background dopants, the volumetric deep defect density (N_t) is the difference between these values,[32,51] yielding N_t of 3.196×10^{13} cm^{-3}. Moreover, the dynamic shunt resistance (R_{sh}) was extracted from the dark I–V characteristics (Figure 1a) near zero bias, yielding a value of 0.89 MΩ. This finite sub-megaohm shunt resistance confirms the presence of parasitic parallel leakage pathways.[52,53] Together, these quantitative measurements of interface and bulk deep traps imply that trap-mediated recombination by Shockley–Read–Hall (SRH) mechanisms is the primary phenomenon driving the measured ideality factor of ~2.5.

Conclusions

In this work, we demonstrate a simple method to fabricate a p–n near-IR photodetector based on a n-$MoSe_2/MoS_2$ thin film integrated with a commercial p-Si wafer via RF sputtering, operating at room temperature. Our device's fabrication process is scalable, achieves compelling interface quality, and does not require mechanical exfoliation of TMDC layers; moreover, the device demonstrates proportional generation of current under incident illumination at 980-nm and 808-nm wavelengths under reverse bias with moderate metrics of detectivity (1.1×10^5 Jones) and responsivity (0.045 μA W^{-1}). Our device presents an ideality factor of ~2.5, which correlates with a high volumetric defect density and interface trap density, strongly suggesting a Shockley–Read–Hall (SRH) recombination process. The device can operate as a self-powered device with maximum photogenerated currents of 16 nA and detectivities and responsivities one order of magnitude lower than in the reverse-bias operation. These results indicate that p-Si/$MoSe_2$/MoS_2 heterojunction devices are promising structures for low-power, low-cost, near-IR photodetection applications.

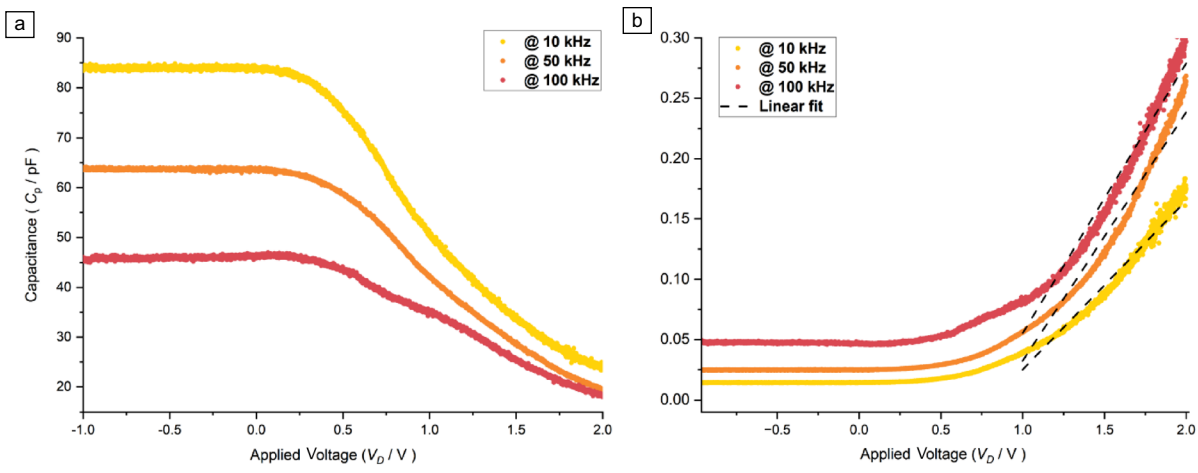


Figure 5. (a) Capacitance versus applied voltage at different frequencies, (b) and Mott–Schottky plot of $1/C^2$ versus applied voltage in the frequency range of 10 to 100 kHz. Voltage applied to the top contact relative to the p-type silicon substrate.

Methods

Sample preparation

We used RF sputtering to fabricate the $MoS_2/MoSe_2$ multilayer thin film on a Kurt J. Lesker PVD 75 machine, utilizing commercial targets with 99.9% purity, following previous works.[25,28] The fabrication of thin films was achieved at room temperature. MoS_2 and $MoSe_2$ exhibit an intrinsically *n*-type semiconductor character, primarily attributed to sulfur vacancies and dangling bonds at the grain-boundary edges.[54,55] Thus, the $MoS_2/MoSe_2$ multilayer thin film consists of a *nn* heterojunction. The substrate was a commercial *p*-type Si wafer (⟨100⟩, 0.01–0.05 Ω cm) with a diameter of 10.16 cm and a thickness of 500 µm, and the $MoS_2/MoSe_2$ multilayer thin film was deposited directly on it. The fabrication process consists of a two-step, sequential deposition of MoS_2 after $MoSe_2$, without breaking the vacuum, to achieve a high-quality, contaminant-free $MoS_2/MoSe_2$ multilayer thin film. During fabrication, we set the vacuum pressure to 1×10^{-4} Pa and the RF power to 200 W at 13.56 MHz. The deposition rate was ~0.3 nm/s to achieve the thickness of the MoS_2 and $MoSe_2$ of ~800 nm each, resulting in a total film thickness of ~1.6 µm. The final device was obtained by cutting the Si substrate into 25.4×25.4 mm^2 dice.

Structural characterization

SEM

We employed a Nova 600 Nanolab SEM from FEI Company, setting a tilt angle of 45° with a working voltage of 5 kV to avoid damage to the material, and a working distance of 4.4 mm with magnifications of 15,000× and 30,000×.

Raman spectroscopy

Raman spectroscopy was performed using a Horiba Raman Spectrometer Olympus BX41 equipped with a 532-nm laser. The measurements consisted of 10 accumulations with an acquisition time of 1 s and a grating of 1800 gr/mm at 10% laser power. Raman spectroscopy was performed at room temperature without further sample preparation.

Atom probe tomography

The chemical elemental distribution was studied using a Cameca® Local Electrode Atom Probe (LEAP 4000X HR) system equipped with a UV laser (~355 nm). The measurements were obtained under ultrahigh vacuum at 50 K with a detection rate of 0.2%, a pulse frequency of 125 kHz, and a laser beam energy of 20 pJ. The films were directly sputtered onto preshaped Si tips. All data were reconstructed with Cameca AP Suite 6.3. The proxigram was obtained with a bin size of 0.1 nm and a maximum distance of 6 nm.

Electrical characterization

We used a Keithley Source Meter Unit (SMU) 2400 to record the *I–V* measurements for our devices. The comparison between the two-wire local sensing (2WLS) and four-wire remote sensing (4WRS) configurations for recording *I–V* measurements showed no significant difference between these two configurations. Therefore, to ease the measurement setup, we employed the 2WLS configuration only, as reported in previous works.[35] To avoid a photo-thermoelectric effect at the metal–semiconductor interface causing the detected current, rather than the separation of photo-excited electron–hole pairs, as reported by Buscema et al.,[56] we located new W probe tips away from the laser spot, and we avoided using deposited metal contacts on the device. The tips were placed until they gently touched the device's surface. These tips were also spaced ~2 cm from each other at the extremes of the device. We employed two commercial spot laser diodes with wavelengths of 980 and 808 nm, with variable power as a function of applied voltage. The laser spot for each laser was ~2 µm. This laser's wavelength corresponds to energies of 1.2 and 1.5 eV, which are close to the expected bandgap of the $MoS_2/MoSe_2$ heterojunction and can excite electron–hole pairs at the junction. To evaluate the response time of our device, we used the evaluation of the time difference between the 10 and 90% steady-state photocurrent thresholds.

For capacitance versus voltage measurements, we employed a Keithley 4200 semiconductor parameter analyzer equipped with the 4215 CVU module. Measurements were taken under dark and ambient temperature conditions with forward bias applied to the anode of the device.

Acknowledgments

O.A.L.-G. thanks the support from Secretaría de Ciencia, Humanidades, Tecnología e Innovación (SECIHTI) from Mexico for the postdoctoral fellowship. All authors greatly acknowledge the support of R.C. Ambrosio Lázaro and C. Ascencio from Benemérita Universidad Autónoma de Puebla (BUAP) for their assistance and fruitful discussion of the electrical measurements. All authors acknowledge the support of D.V. Pete at CINT for his assistance with scanning electron microscopy characterization. M.R. and O.A.L.G. thank the Sistema Nacional de Investigadoras e Investigadores program from SECIHTI, and Dirección General de Investigación y Transferencia Tecnológica (DGITT) from Universidad Autónoma de Ciudad Juárez (UACJ). This work was performed, in part, at the Center for Integrated Nanotechnologies, an Office of Science User Facility operated for the US Department of Energy (DOE) Office of Science. Sandia National Laboratories is a multimission laboratory managed and operated by National Technology & Engineering Solutions of Sandia, LLC, a wholly owned subsidiary of Honeywell International, Inc., for the US DOE's National Nuclear Security Administration under contract DE-NA-0003525. The views expressed in the article do not necessarily represent the views of the US DOE or the United States Government.

Author contributions

O.A.L.G. completed conceptualization, principal research, and original draft writing. O.A.L.G. and J.N. performed device fabrication. O.A.L.G., N.P., and D.N. performed electrical measurements and analysis. D.C. and P.M.P. aided with the APT measurements and analysis. N.P., M.R., A.C., M.H., M.T., and M.R. provided revision and research guidance. All authors reviewed the final version of this manuscript.

Funding

Secretaría de Ciencia, Humanidades, Tecnología e Innovación (Secihti) from Mexico for the postdoctoral fellowship "Estancia Posdoctoral por México" number 790769. Project PIISO23-IIT-05 from Universidad Autónoma de Ciudad Juárez (UACJ). The Center for Integrated Nanotechnologies (CINT) proposal number 2023BU0045.

Data availability

The data that support the findings of this study are available from the corresponding author upon reasonable request.

Conflict of interest

The authors have no conflicts of interest to disclose.

Supplementary Information

The online version contains supplementary material available at https://doi.org/10.1557/s43577-026-01233-5.

Open Access

This article is licensed under a Creative Commons Attribution 4.0 International License, which permits use, sharing, adaptation, distribution and reproduction in any medium or format, as long as you give appropriate credit to the original author(s) and the source, provide a link to the Creative Commons licence, and indicate if changes were made. The images or other third party material in this article are included in the article's Creative Commons licence, unless indicated otherwise in a credit line to the material. If material is not included in the article's Creative Commons licence and your intended use is not permitted by statutory regulation or exceeds the permitted use, you will need to obtain permission directly from the copyright holder. To view a copy of this licence, visit http://creativecommons.org/licenses/by/4.0/.

References

1. G. Simone, R.D. Di Carlo, X. De Vries, G.H.L. Heintges, S.C.J. Meskers, R.A.J. Janssen, G.H. Gelinck, *Adv. Mater.* **30**, 1804678 (2018). https://doi.org/10.1002/adma.201804678
2. Q. Wang, Y. Zhang, Z. Wei, *Chin. J. Chem.* **41**, 958 (2023). https://doi.org/10.1002/cjoc.202200686
3. M.I. Saleem, A.K.K. Kyaw, J. Hur, *Adv. Opt. Mater.* **12**, 2401625 (2024). https://doi.org/10.1002/adom.202401625
4. Z. Cheng, T. Zhao, H. Zeng, *Small Sci.* **2**, 2100051 (2022). https://doi.org/10.1002/smsc.202100051
5. Y. Wang, X. Zhang, S. Wang, Z. Chen, P. Zhang, F. Yang, W. Zhao, J. Lu, H. Liu, *Appl. Phys. Lett.* **127**, 033104 (2025). https://doi.org/10.1063/5.0279492
6. R.K. Bhan, V. Dhar, *Opto-Electron. Rev.* **27**, 174 (2019). https://doi.org/10.1016/j.opelre.2019.04.004
7. P. Martyniuk, A. Rogalski, *Opto-Electron. Rev.* (2013). https://doi.org/10.2478/s11772-013-0090-x
8. R. Ambrosio, M. Moreno, J. Mireles Jr., A. Torres, A. Kosarev, A. Heredia, *Phys. Stat. Solidi C* **7**, 1180 (2010). https://doi.org/10.1002/pssc.200982781
9. X. Wen, W. Lei, W. Tang, B. Di, G. Zhang, Y. Zhang, H. Chang, W. Zhang, *ACS Appl. Mater. Interfaces* **17**, 40682 (2025). https://doi.org/10.1021/acsami.5c06677
10. M. Moun, M. Kumar, M. Garg, R. Pathak, R. Singh, *Sci. Rep.* **8**, 11799 (2018). https://doi.org/10.1038/s41598-018-30237-8
11. C.K. Zankat, P.M. Pataniya, A. Patel, S.A. Bhakhar, S. Narayan, G.K. Solanki, K.D. Patel, V.M. Pathak, C.K. Sumesh, P.K. Jha, *Mater. Today Energy* **18**, 100550 (2020). https://doi.org/10.1016/j.mtener.2020.100550
12. M. Dai, Q. Wu, C. Wang, X. Liu, X. Zhang, Z. Cai, L. Lin, X. Gu, K. Ostrikov, H. Nan, S. Xiao, *Adv. Opt. Mater.* **12**, 2301900 (2024). https://doi.org/10.1002/adom.202301900
13. G.H. Shin, J. Park, K.J. Lee, G.-B. Lee, H.B. Jeon, Y.-K. Choi, K. Yu, S.-Y. Choi, *ACS Appl. Mater. Interfaces* **11**, 7626 (2019). https://doi.org/10.1021/acsami.8b21629
14. J. Zha, M. Luo, M. Ye, T. Ahmed, X. Yu, D. Lien, Q. He, D. Lei, J.C. Ho, J. Bullock, K.B. Crozier, C. Tan, *Adv. Funct. Mater.* **32**, 2111970 (2022). https://doi.org/10.1002/adfm.202111970
15. J.K. Joseph, T. Lavanya, K. Naresh, S. Suneetha, R. Thangavel, A. Karthigeyan, K. Thangaraju, *Thin Solid Films* **834**, 140853 (2026). https://doi.org/10.1016/j.tsf.2026.140853
16. S. Lee, J. Shin, J. Jang, *Adv. Funct. Mater.* **27**, 1604921 (2017). https://doi.org/10.1002/adfm.201604921
17. Q. Zhao, R. Tang, S. Yang, T. Chen, *Adv. Sci.* **12**, e11387 (2025). https://doi.org/10.1002/advs.202511387
18. A. Amin, C. Cagno, Y. Wang, F. Yan, *Solar RRL* **9**, 2500330 (2025). https://doi.org/10.1002/solr.202500330
19. A. Ali, B. Kadiri-English, D. Son, J. Lee, J. Kang, D. Hwang, S. Sung, K. Yang, D. Kim, *Solar RRL* **9**, e202500685 (2025). https://doi.org/10.1002/solr.202500685
20. C.-C. Chung, H. Yeh, P.-H. Wu, C.-C. Lin, C.-S. Li, T.-T. Yeh, Y. Chou, C.-Y. Wei, C.-Y. Wen, Y.-C. Chou, C.-W. Luo, C.-I. Wu, M.-Y. Li, L.-J. Li, W.-H. Chang, C.-W. Chen, *ACS Nano* **15**, 4627 (2021). https://doi.org/10.1021/acsnano.0c08970
21. Q.-H. Zhu, J. Chai, S.-Y. Wei, J.-B. Sun, Y.-J. Sun, D. Kiriya, M.-S. Xu, *Nanomaterials* **15**, 519 (2025). https://doi.org/10.3390/nano15070519
22. I.R. Chávez-Urbiola, F.J. Willars-Rodríguez, R. Ramírez Bon, P. Vorobiev, Yu.V. Vorobiev, *Thin Solid Films* **669**, 364 (2019). https://doi.org/10.1016/j.tsf.2018.10.002
23. A.A.A. Khalil, A.M. Karmalawi, A.A. Abdelmageed, F. Mohamed El-Sharkawy, E. Mousa, H.A.S. Al-shamiri, H.A. Shawkey, M.T.H. Abou Kana, H.M. Kandel, M.A. Swillam, *Opt. Mater.* **150**, 115168 (2024). https://doi.org/10.1016/j.optmat.2024.115168
24. M. Ma, H. Chen, K. Zhou, C. Xie, Y. Liang, L. Wang, C. Wu, W. Yang, J. Guo, L. Luo, *J. Mater. Chem. C* **9**, 2823 (2021). https://doi.org/10.1039/D0TC05701K
25. M. Ramos, J. Nogan, M. Ortíz-Díaz, J.L. Enriquez-Carrejo, C.A. Rodriguez-González, J. Mireles-Jr-Garcia, C. Ornelas, A. Hurtado-Macias, *Surf. Topogr. Metrol. Prop.* **5**, 025003 (2017). https://doi.org/10.1088/2051-672X/aa7421
26. J. Jaiswal, A. Das, V. Chetry, S. Kumar, R. Chandra, *Sens. Actuators, B Chem.* **359**, 131552 (2022). https://doi.org/10.1016/j.snb.2022.131552
27. Z.-H. Chi, X.-M. Zhao, H. Zhang, A.F. Goncharov, S.S. Lobanov, T. Kagayama, M. Sakata, X.-J. Chen, *Phys. Rev. Lett.* **113**, 036802 (2014). https://doi.org/10.1103/PhysRevLett.113.036802
28. O.A. López-Galán, T. Boll, J. Nogan, D. Chassaing, A. Welle, M. Heilmaier, M. Ramos, *Sci. Rep.* **14**, 7104 (2024). https://doi.org/10.1038/s41598-024-57243-3
29. A. Fajardo-Peralta, M.A.T. Nguyen, J. Valenzuela-Benavides, A. Brodie, R.N. Gontijo, A.L. Elías, N. Perea-Lopez, T.E. Mallouk, M. Terrones, *Mater. Res. Express* **9**, 046301 (2022). https://doi.org/10.1088/2053-1591/ac5ef3
30. M. Ramos, J. Nogan, T. Boll, S. Kauffmann-Weiss, C.A. Rodriguez-Gonzalez, J.L. Enriquez-Carrejo, M. Heilmaier, *MRS Commun.* **9**, 1261 (2019). https://doi.org/10.1557/mrc.2019.150
31. Z. Wang, Y. Chen, P. Wu, J. Ye, M. Peng, Y. Yan, F. Zhong, T. He, Y. Wang, M. Xu, K. Zhang, Z. Hu, Q. Li, L. Zhang, F. Wang, P. Wang, *Infrared Phys. Technol.* **106**, 103272 (2020). https://doi.org/10.1016/j.infrared.2020.103272
32. S. Srivastava, Y.N. Mohapatra, *J. Appl. Phys.* **129**, 205702 (2021). https://doi.org/10.1063/5.0048592
33. T.K.H. Pham, B.Q. Tran, K.B. Nguyen, N.Y.N. Pham, T.H.Y. Nguyen, A.H.-T. Nguyen, N.P. Nguyen, H.D. Ngo, H.P. Pham, *Mater. Adv.* **6**, 1719 (2025). https://doi.org/10.1039/D4MA01113A
34. D. Roy, S.N. Riaz, A. Banerjee, S. Bhattacharjee, S. Sarkar, K.K. Chattopadhyay, *ACS Appl. Mater. Interfaces* **17**, 27497 (2025). https://doi.org/10.1021/acsami.5c03700
35. R. Ginige, K. Cherkaoui, V. Wong Kwan, C. Kelleher, B. Corbett, *J. Appl. Phys.* **95**, 2809 (2004). https://doi.org/10.1063/1.1644905
36. J.M. Shah, Y.-L. Li, T. Gessmann, E.F. Schubert, *J. Appl. Phys.* **94**, 2627 (2003). https://doi.org/10.1063/1.1593218

37. Z. Lin, W. Liu, S. Tian, K. Zhu, Y. Huang, Y. Yang, *Sci. Rep.* **11**, 7037 (2021). https://doi.org/10.1038/s41598-021-86479-6
38. D.-S. Tsai, K.-K. Liu, D.-H. Lien, M.-L. Tsai, C.-F. Kang, C.-A. Lin, L.-J. Li, J.-H. He, *ACS Nano* **7**, 3905 (2013). https://doi.org/10.1021/nn305301b
39. M. Kumar, S. Rani, A. Pandey, K.S. Gour, S. Husale, P. Singh, V.N. Singh, *J. Alloy. Compd.* **838**, 155384 (2020). https://doi.org/10.1016/j.jallcom.2020.155384
40. E.P. Mukhokosi, S.B. Krupanidhi, K.K. Nanda, *Phys. Stat. Solidi A* **215**, 1800470 (2018). https://doi.org/10.1002/pssa.201800470
41. S. Ghosh, P. Venkatram, H. Ravichandran, R.T. Nair, Y. Sun, L. Ding, C. Chen, J.M. Redwing, Y. Yang, S. Das, *Nat. Electron.* **9**, 775 (2026). https://doi.org/10.1038/s41928-026-01624-1
42. W. Choi, M.Y. Cho, A. Konar, J.H. Lee, G. Cha, S.C. Hong, S. Kim, J. Kim, D. Jena, J. Joo, S. Kim, *Adv. Mater.* **24**, 5832 (2012). https://doi.org/10.1002/adma.201201909
43. J. Ning, Y. Zhou, J. Zhang, W. Lu, J. Dong, C. Yan, D. Wang, X. Shen, X. Feng, H. Zhou, Y. Hao, *Appl. Phys. Lett.* **117**, 163104 (2020). https://doi.org/10.1063/5.0020771
44. L. Zeng, S. Lin, Z. Lou, H. Yuan, H. Long, Y. Li, W. Lu, S.P. Lau, D. Wu, Y.H. Tsang, *NPG Asia Mater* **10**, 352 (2018). https://doi.org/10.1038/s41427-018-0035-4
45. S.V. Desarada, S. Chaure, N.B. Chaure, *Mater. Today Commun.* **39**, 109160 (2024). https://doi.org/10.1016/j.mtcomm.2024.109160
46. A. Rasyotra, S. Ghosh, R.T. Nair, P. Venkatram, A. Chowdhury, M.S. Alam, J.M. Kumar, K. Mukhopadhyay, S. Das, *Nat. Sens.* **1**, 305 (2026). https://doi.org/10.1038/s44460-026-00042-2
47. H. Ferhati, F. Djeffal, A. Bendjerad, L. Foughali, A. Benhaya, A. Saidi, *J. Alloy. Compd.* **907**, 164464 (2022). https://doi.org/10.1016/j.jallcom.2022.164464
48. S.S. Kumar, S. Valanarasu, M.A. Manthrammal, S. Mohd, *J. Mater. Sci. Mater. Electron.* **35**, 195 (2024). https://doi.org/10.1007/s10854-023-11820-w
49. D.C. Tripathi, Y.N. Mohapatra, *Appl. Phys. Lett.* **102**, 253303 (2013). https://doi.org/10.1063/1.4812487
50. R. Ramadan, R.J. Martín-Palma, *Energies* **13**, 2165 (2020). https://doi.org/10.3390/en13092165
51. H.F. Haneef, A.M. Zeidell, O.D. Jurchescu, *J. Mater. Chem. C* **8**, 759 (2020). https://doi.org/10.1039/c9tc05695e
52. B.L. Williams, S. Smit, B.J. Kniknie, K.J. Bakker, W. Keuning, W.M.M. Kessels, R.E.I. Schropp, M. Creatore, *Prog. Photovoltaics Res. Appl.* **23**, 1516 (2015). https://doi.org/10.1002/pip.2582
53. S. Kumar, D. Gahlawat, J. Kaur, U. Rani, J. Madan, R. Pandey, R. Basu, *Opt. Quant. Electron.* **57**, 571 (2025). https://doi.org/10.1007/s11082-025-08487-4
54. M. Ramos, O.A. López-Galán, J. Polanco, M. José-Yacamán, *Materials* **15**, 6732 (2022). https://doi.org/10.3390/ma15196732
55. S. McDonnell, R. Addou, C. Buie, R.M. Wallace, C.L. Hinkle, *ACS Nano* **8**, 2880 (2014)
56. N. Perea-López, Z. Lin, N.R. Pradhan, A. Iñiguez-Rábago, A. Laura Elías, A. McCreary, J. Lou, P.M. Ajayan, H. Terrones, L. Balicas, M. Terrones, *2D Mater.* **1**, 011004 (2014). https://doi.org/10.1088/2053-1583/1/1/011004

Publisher's note
Springer Nature remains neutral with regard to jurisdictional claims in published maps and institutional affiliations.